minerals

MDPI

Article

Structural Assessment of Fluorine, Chlorine, Bromine, Iodine, and Hydroxide Substitutions in Lead Arsenate Apatites (Mimetites)–$Pb_5(AsO_4)_3X$

Julia Sordyl [1,*], Bartosz Puzio [1], Maciej Manecki [1], Olaf Borkiewicz [2], Justyna Topolska [1] and Sylwia Zelek-Pogudz [1]

[1] Faculty of Geology, Geophysics and Environmental Protection, AGH-University of Science and Technology, al. Mickiewicza 30, 30-059 Kraków, Poland; bpuzio@agh.edu.pl (B.P.); gpmmanec@cyf-kr.edu.pl (M.M.); topolska@agh.edu.pl (J.T.); zelek@geol.agh.edu.pl (S.Z.-P.)

[2] X-ray Science Division, Advanced Photon Source, Argonne National Laboratory, Argonne, Illinois 60439, United States; borkiewicz@aps.anl.gov (O.B.)

* Correspondence: sordyljulia@gmail.com

Received: date; Accepted: date; Published: date

Abstract: Five lead-arsenate apatites (mimetites) - $Pb_5(AsO_4)_3X$, where X denotes fluorine (F), chlorine (Cl), bromine (Br), iodine (I), and hydroxide (OH), were synthesized via precipitation from aqueous solutions. The crystal structures were determined through Rietveld refinement of powder synchrotron X-ray data. All the compounds crystallized in the hexagonal class symmetry (space group $P6_3/m$). The Rietveld refinement indicated that mimetite-Cl, -Br, -I, and –OH had an anion deficiency at position X. Substitution of halogens in a mimetite structure brought about systematic changes in unit-cell parameters, interatomic distances, and metaprism twist angles φ, proportional to the substituted halogen's ionic radius. Mimetite-OH did not follow the linear correlations determined within the series. Twist angle φ, a useful device for monitoring changes in apatite topology, ranged from 20.34° for mimetite-F to 11.42° for mimetite-I. The geometric method has been proposed for determining the diameter of hexagonal channels hosting halogens in apatites. A comparison of the results with halogenated pyromorphites showed similar systematic trends: the substitutions in mimetites have comparable effect on the interatomic distances as in their phosphorous analogues.

Keywords: halogenated mimetites; Rietveld refinement; synchrotron; anionic substitution; twist angle

1. Introduction

The crystal structure and crystal chemistry of apatites have been analyzed in detail in recent reviews [1-5, and the literature cited therein]. Briefly, the generalized formula of apatite is written as $[M(1)]_2[M(2)]_3(TO_4)_3X$. The basic apatite structure is predominantly hexagonal with space group $P6_3/m$, although a few monoclinic forms have also been reported. Oxide ions occupy two special positions O(1) and O(2) and one general position O(3) around the T site. Usually, the $M(1)$ and $M(2)$ site cations are divalent (e.g. Ca^{2+}, Pb^{2+}, Sr^{2+}, Ba^{2+}), the T cation is pentavalent (e.g. P^{5+}, As^{5+}, V^{5+}), and the X anion monovalent (e.g. OH^-, F^-, Cl^-, Br^-, I^-). However, the apatite lattice is very tolerant of substitution. Hence, charge neutrality can also be maintained by other ions (CO_3^{2-}, REE^{3+}, S^{6+}, Si^{4+}, Na^+, etc.) and by vacancies [6].

In an apatite structure with a space group symmetry $P6_3/m$, a hexagonal atomic framework is based on two distinct metal-cation sites -- $M(1)$ and $M(2)$, a tetrahedral-cation site (T), and an anion column along four edges of the unit cell. The tetrahedral site is a TO_4 tetrahedron. The $M(1)$ site is an $M(1)O_9$ tricapped-trigonal prism, while the $M(2)$ site is an irregular $M(2)O_6X_1$ polyhedron. The X

anions exist in (0,0,*z*) columns along the edges of the unit cell [7] (see also White et al., [3] for a detailed description of apatite structures). The location of *X* anion with respect to the surrounding *M*(2) cations has been thoroughly described in various research studies [8-11]. It has been shown that in the case of $Ca_{10}(PO_4)_6F_2$, F fits within a Ca(2) triangle, while OH, Cl, and Br substitutions subsequently lead to a greater displacement out of the triangular plane [3]. Kim et al., [11] demonstrated that despite the larger size of the Pb(2) triangles as compared to Ca(2) triangles, Cl and F are also displaced away from the triangular plane, whereas, for the F-, Cl-, and Br- lead apatites, the anions were found to be at the (0,0,½) position.

Little is known about the apatite with I in position *X*, but the iodine vanadinite $Pb_5(VO_4)_3I$ is well documented [12-15]. The iodine mimetite - $Pb_5(AsO_4)_3I$ was synthesized by Merker and Wondratschek, [16]. The scientists have proposed that the large size of the I^- anion prevents the creation of the iodine-phosphate apatite. Monovalent anions *X* occupy hexagonal channels, which extend along the crystallographic axis *c* in the apatite structure. These channels have given the apatite group the name -- mesoporous solids [17]. Some authors find that the larger size of a unit cell enables the incorporation of a halogen with a larger ionic radius [4,18]. However, this proposition seems to be speculative as the parameter *c* of both calcium and strontium apatites decreases with the replacement of systematically larger halogen anions [11,17,19].

Several chemical analyses of natural apatite supergroup minerals formed in the oxidation zone indicate that the elemental composition of apatites mirrors the composition of the aqueous solutions from which they precipitate [18,20]. Several synthesis experiments have also shown that the composition of products can be accurately controlled by the composition of the initial solutions [11,17,21-28]. Hence, induced apatite precipitation can be used to immobilize pollutants in contaminated soils, waste, or waters. Anthropogenic emissions of lead and arsenic from industrial processes and the processing of mineral resources pose a threat to human health and the environment. In the 1990s, the in-situ immobilization of lead technique was developed [29-34]. Over time, this remediation technique has developed into the Phosphate Induced Metal Stabilization technique [35-38]. Furthermore, catastrophic contamination of drinking water by arsenic in the Indian subcontinent, Cambodia, and Bangladesh is well documented, and studies have been conducted over the years to devise methods for removal of arsenic from drinking water using hydroxylapatites and similar materials, including bone meal [39-42].

Minerals from the apatite group have also been proposed for use in the storage of nuclear waste, containing I, Cs, Sr, rare earth elements and actinides [43-47]. However, isotope ^{129}I is particularly challenging as it has a long half-life of 1.57×10^7 years, and iodine in reduced I^- form is highly mobile in the environment. Materials with a crystalline apatite structure have a high potential to bind ^{129}I due to their strength, durability, low solubility, and relatively high iodine content, which lowers the rate of iodine release and minimizes the volume of waste. To optimize the storage efficiency of such nuclear wastes, the properties of synthetic apatite compositions containing I should be studied. To date, very few phases have been synthesized experimentally [14,48-51]

Hence, the systematization of the chemistry and crystal structure of different apatites is essential for functionally adapting it to specific technologies. This requires, among others, accurate descriptions of the crystal structures. For this purpose, single-crystal analysis is preferred, however, many apatites are easily synthesized in powder form and the Rietveld refinement procedure is very widely used in such cases. Nevertheless, the least-squares method, used during the Rietveld refinement, can result in false minima due to the propagation of errors [52]. In such cases, the application of restraints on TO_4 tetrahedra or selected bond lengths or atomic positions is used [53,54].

This paper presents the synthesis of several lead-arsenic apatites (mimetites) containing F, Cl, Br, I, and OH ions on the anionic sites. The syntheses were made from aqueous solutions, which provided both mineralogical and environmental significance to the results. For the first time, systematic variations in mimetite structure brought about by anionic substitutions in *X* position in such a wide range of substitutions have been thoroughly described. The analysis of the structure by

Rietveld refinement of synchrotron data, which is the state-of-the-art solution for fine crystalline products of synthesis from aqueous solutions, is presented. The syntheses were performed based on the unified procedure and under the same conditions. This ensured that the presented systematic changes in the structures of the studied phases resulted solely from the substitutions on anionic sites and were not affected by the method of crystallization. To our knowledge, no accurate structural studies of the halogen-substituted lead-arsenate apatites have been reported to date.

2. Materials and Methods

2.1. Synthesis

The following five phases of arsenate-lead apatites (mimetites) were synthesized by precipitation from aqueous solutions using a modified Baker, [55] method: $Pb_5(AsO_4)_3F$, $Pb_5(AsO_4)_3Cl$, $Pb_5(AsO_4)_3Br$, $Pb_5(AsO_4)_3I$, and $Pb_5(AsO_4)_3OH$. The syntheses were carried out at 25°C, by the dropwise addition (at a rate of 2 mL/min) of aqueous solutions of $Pb(NO_3)_2$, $Na_2AsHO_4{\cdot}7H_2O$, and one of the following: NH_4F, NaCl, NH_4Br, or KI. The Pb/As and As/*X* (where *X* = F, Cl, Br, I, and OH) molar ratios in the mixed solutions were maintained at 1.67 and 3.00, respectively. All the samples were synthesized at pH = 4.5, open to the air and atmospheric carbon dioxide (CO_2). The pH was maintained throughout the experiments using a 0.1 M solution of NH_4OH or HNO_3. The precipitates were aged in a suspension for 72 h, centrifuged, and washed with double-distilled water.

2.2. Analytical methods

Solid characterization with scanning electron microscopy (SEM) was carried out at a low vacuum for the uncoated samples using an FEI Quanta 200 FEG SEM (Hillsboro, OR, USA) equipped with secondary-electron and back-scattered-electron detectors. Energy dispersive spectrometry (EDS, FEI Quanta) was employed to monitor variations in the chemical composition.

Conventional powder X-ray diffraction patterns were recorded with the Rigaku SmartLab diffractometer (Neu-Isenburg, Tokyo, Japan) using graphite-monochromatized CuKα radiation, an operating voltage of 45 kV, a current of 200 mA in a 3° to 73°2θ range, a step size of 0.02°, and a counting time of 1s/step. The samples were ground prior the measurements using a pestle and mortar. The phases were identified using the ICCD database and XRAYAN software [56]. Preliminary unit-cell parameters were calculated from powder XRD patterns using UnitCell software [57] for the hexagonal crystal system (space group $P6_3/m$) based on the position of up to 17 diffraction lines.

For synchrotron X-ray diffraction the powders were ground using a pestle and mortar and sieved through a 20-μm sieve. High-resolution X-ray diffraction data were collected at beamline 11-BM of the Advanced Photon Source, Argonne National Laboratory. To decrease the absorption coefficient of samples containing high-Z elements, effective packed density have been reduced by limiting the amount of sample present in the X-ray beam; a fine layer of material has been spread on the outside of a 0.8-mm Kapton capillary using low-density wax as "adhesive", which in turn was sleeved into a 1.1-mm capillary and mounted to a modified 11-BM bases. Bases have been mounted onto beamline goniometer equipped with high-speed spinner, ensuring excellent powder averaging. Samples were measured in transmission geometry using photon energy of 0.4128 Å with the scattered intensities recorded by multi-analyzer detector system consisting of 12 independent Si (111) crystal analyzers and $LaCl_3$ scintillation detectors, spaced 2º apart. A pair of slits between the sample and each crystal is used to separate and collimate the diffracted beam from the sample. This multianalyzer/detector scheme enables simultaneous high-speed (~1 hour) and high-resolution ($\Delta Q/Q \approx 2\times10^{-4}$) data collection. Discrete detectors covering an angular range from −6 to 16° 2θ were scanned over a 34° 2θ range, with data points collected every 0.001° 2θ at a speed of 0.01° s−1 while continually scanning the diffractometer 2θ arm. A mixture of NIST standard reference materials, Si (SRM 640c) and Al2O3 (SRM 676) was used to calibrate the instrument. Corrections were applied for detector sensitivity, 2θ offset, small differences in wavelength between detectors, and the source

intensity, as noted by the ion chamber before merging the data into a single set of intensities evenly spaced in 2θ. All the refinements were performed with the help of the General Structure Analysis System (GSAS) program of Larson and Von Dreele, [58] using the EXPGUI interface of Toby, [59]. Molecular graphics was performed using VESTA software [60]. Structural refinement was performed using the Rietveld method [61]. The initial coordinates were taken from pyromorphite $Pb_5(PO_4)_3Cl$ determined by Dai and Hughes, [62]. The refinement parameters included the scale factor and 36 background terms in a Chebyshev first-order polynomial. Peak profiles were modelled using the pseudo-Voigt profile function which includes the Stephens model for anisotropic strain broadening (Type 4). Number of peaks equaled to: 2060, 2127, 2158, 2195, and 2122 for mimetite-F, -Cl, -Br, -I, and -OH, respectively. The initial unit-cell parameters were calculated using conventional X-ray powder diffraction data. The final unit-cell dimensions were refined after convergence for the aforementioned parameter was achieved. Soft constraints were imposed on the As – O bond lengths. The atomic position *z* for anion *X* was fixed at 1/2 except for OH. Then, the atomic positions, occupancy factors, and isotropic atomic displacement factors were modelled.

To evaluate the Pb and As molar ratio in the obtained materials, the full chemical composition was determined using Inductively Coupled Plasma-Optical Emission Spectrometry (ICP-OES) method (Perkin Elmer Optima 7300DV instrument) following prior digestion of samples in concentrated HNO_3 mixed with 0.02M EDTA. The content of F, Br, and I was analyzed using Inductively Coupled Plasma-Mass Spectrometry (ICP-MS). For technical reasons, the content of Cl was determined using SEM/EDS. The OH content was assumed based on the stoichiometry of the ideal formula.

3. Results

3.1. Preliminary characteristics of the synthesized products

The syntheses produced homogeneous, white to cream, fine crystalline powders. The crystals were well developed with sizes between 2 μm and 5 μm (Figure 1). Their hexagonal morphology is typical for apatites. Even though the synthesized products were aged in suspension for 6 days, a smaller population of needle-shaped crystals (<1 μm) was still visible in mimetite-F precipitate (Figure 1). The finest crystals were observed for mimetite-I. Semi-quantitative EDS analysis (Figure 1) along with wet chemical analysis yielded the composition close to the ideal formula of each crystalline phase (Table 1).

Table 1. Chemical composition of synthetic mimetites.

Intended Chemical Formula	Empirical Chemical Formula	Sample Name
$Pb_5(AsO_4)_3F$	$Pb_{5.00}(AsO_4)_{2.99}F_{0.98}$	mimetite-F
$Pb_5(AsO_4)_3Cl$	$Pb_{5.00}(AsO_4)_{2.99}Cl_{1.00}$	mimetite-Cl
$Pb_5(AsO_4)_3Br$	$Pb_{5.00}(AsO_4)_{2.98}Br_{0.97}$	mimetite-Br
$Pb_5(AsO_4)_3I$	$Pb_{5.00}(AsO_4)_{3.03}I_{0.60}$	mimetite-I
$Pb_5(AsO_4)_3OH$	$Pb_{5.00}(AsO_4)_{3.01}OH_{1.00}$	mimetite-OH

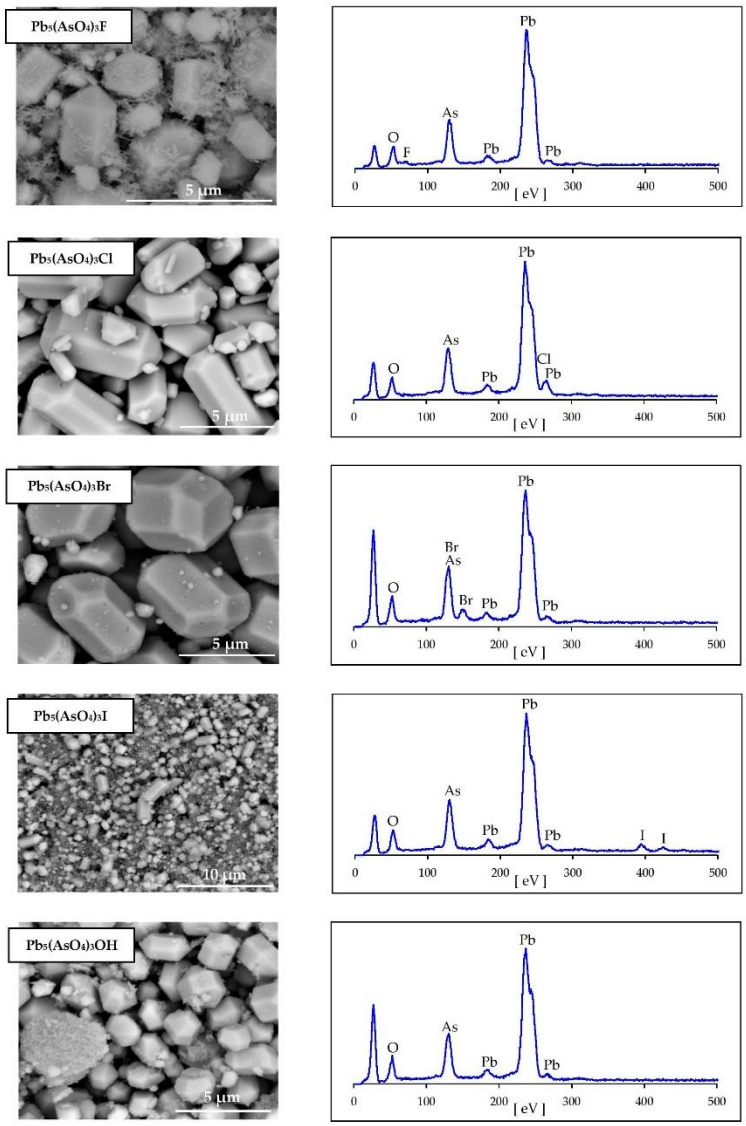

Figure 1. Scanning electron micrographs and EDS elemental analysis of synthesized halogenated mimetites. Unlabeled peak at low eV on EDS spectra is an artifact of mounting (carbon tape).

X-ray diffraction patterns of synthesized phases indicated that the synthesized products were crystalline analogues of Pb-As apatites (Figure 2). No other phases were detected at the detection limit of the method, which is ca. 0.1 wt%. Based on the obtained diffraction patterns and by analogy with other apatites, it was assumed that all synthesized mimetites crystallized in the hexagonal system, in space group $P6_3/m$, ITC No. 176. The position of an intense reflection (*211*) shifted from 29.62°2θ for mimetite-F to 29.41°2θ for mimetite-I, as presented in Figure 2. Systematic shifts of diffraction peaks toward lower 2θ value were apparent with the increase in the helogen's ionic radius, excluding mimetite-OH, which did not follow the trend.

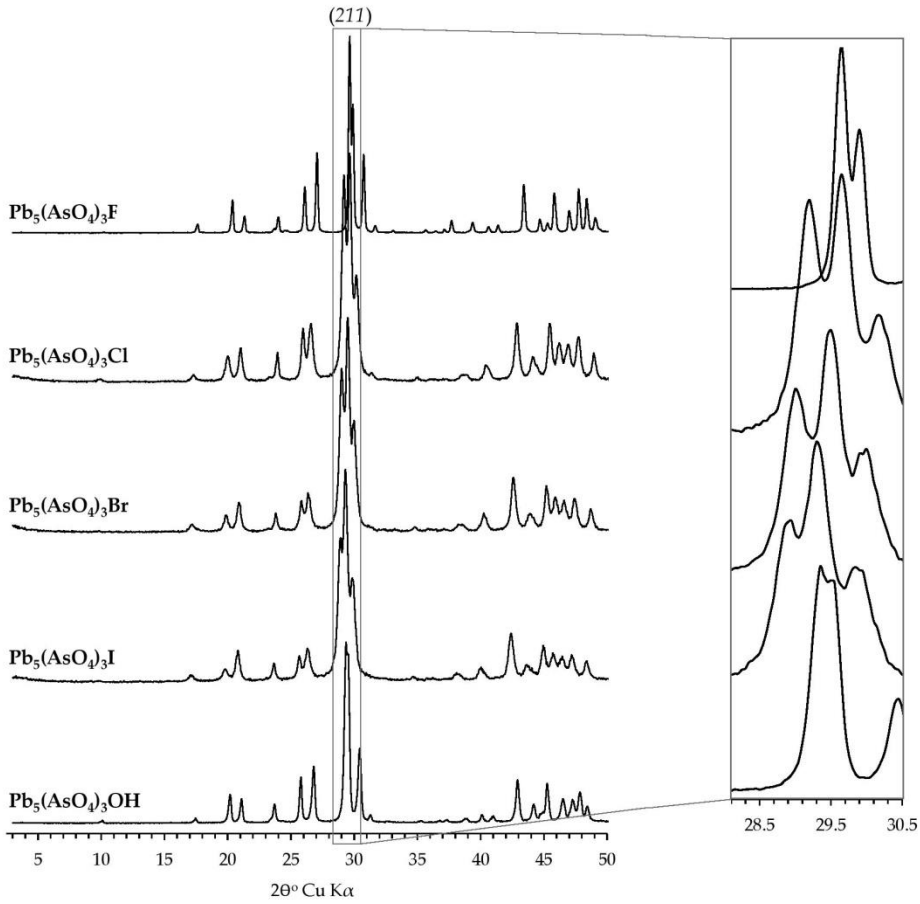

Figure 2. Laboratory X-ray diffraction patterns of synthesized halogenated mimetites. All phases exhibited good crystallinity. No contamination were detected within the detection limit of the method. A systematic shift of peak positions is visible in the inset.

3.2. Rietveld refinement from high-resolution synchrotron data

Structural refinement was performed using the Rietveld method [61]. The initial coordinates were taken from pyromorphite $Pb_5(PO_4)_3Cl$ determined by Dai and Hughes, [62], while the initial unit-cell parameters were calculated using conventional X-ray powder diffraction data. The final refinement parameters are listed in Table 2. The Crystallographic Information Files can be found in the Supplementary Materials (File S1-S5). The atomic positions and atomic displacement parameters along with site occupancy and unit-cell parameters were refined to *wR*p and *R*p below 10% and convergence of the model.

Some authors suggest that in the structural refinements of apatites, TO_4 should be treated as a rigid body to prevent unrealistic bond lengths, and the constraints on the positions of the oxygen atoms should be employed. For instance, structural modelling of mimetite-Cl made by Henderson et al., [17] required restraints of As-O bond length to 1.69 Å in agreement with their EXAFS results. At the same time, Pb-O distances were restrained based on the literature data. Also, Baikie et al., [63] modelled mimetite-Cl structure with several additional manipulations with oxygen atoms to get realistic bond lengths and angles. In this study, although initial modelling without employing the constraints on the bond lengths gave satisfactory fit (wRp < 10 %), the unrealistic As – O bond lengths disqualified these refinements. For this reason, all refinements were attempted whereby a soft constraints were imposed on the As – O bond lengths. They were restrained to be 1.70(1) Å for As – O(1), 1.71(1) Å for As – O(2), and 1.68(1) Å for As – O(3), according to those for mimetite-Cl reported by Dai et al., [64]. These models gave acceptable bond lengths and angles data. Moreover, the mimetite-Br structure refinement required manual fixing of the x and y positions of O(1) atom:

the positions were manipulated until the twist angle refined to ~16°. This value was predicted from the ideal linear correlation of the twist angle with halogen ionic radius (which is discussed further), thus the refinement yielded a superior result (wRp = 8.38% and Rp = 7.1%).

In all the refinements, the position of halogens was set at (0,0,½). Kim et al., [11] reported that in pyromorphite-F, -Cl, and -Br, which are isostructural with mimetites, halogens are positioned at (0,0,½), outside the triangles delineated by Pb(2) atoms. It was assumed that the position of halogens in mimetites is analogous. The position of the OH group was not constrained and was modelled: the resulting value of z = 0.397(8) indicated that it was positioned closer to the Pb(2) triangular plane. Similar results were previously deduced for $Pb_5(PO_4)_3OH$ [11].

Rietveld refinement results showed that occupancy for Cl, Br, I, and OH ion is below 1, resulting in an unbalanced charge and non-stoichiometric chemical formula of these minerals. This indicated the presence of other ions in the structure. The results of independent spectroscopic measurements using FTIR and Raman spectroscopy indicated the presence of CO_3^{2-} ions in the structure of mimetite-Cl, -Br, and -OH, and the presence of OH^- ion in the structure of mimetite-I (data not shown). Spectroscopic studies of these phases are in progress and the results will be published separately. The substitutions were included in the modelled structures which resulted in an improvement in refinements and almost complete charge balance of the structures. The integration of these ions in the structures had negligible effect on final values of unit-cell parameters and atomic coordinates. The chemical formulae of mimetites obtained from modelling were: $Pb_5(AsO_4)_3F_{1.01}$ (charge imbalance +0.01), $Pb_5(AsO_4)_3Cl_{0.80}(CO_3)_{0.05}$ (charge imbalance -0.10), $Pb_5(AsO_4)_3Br_{0.80}(CO_3)_{0.05}$ (charge imbalance -0.10), $Pb_5(AsO_4)_3I_{0.46}(OH)_{0.62}$ (charge imbalance +0.08), $Pb_5(AsO_4)_3OH_{0.87}(CO_3)_{0.04}$ (charge imbalance -0.05). The highest charge imbalance was observed for mimetite-Cl and mimetite-Br. The attempts to include in the modelling procedure the occupancies of other ions gave poor Rw and yielded results oscillating in the charge imbalance range from +0.10 to -0.10. This means that due to the limited accuracy of the diffraction data and the limited capability of the modelling procedure better stoichiometric compliance cannot be achieved for these structures.

As presented in Figure 3, tiny, unidentified peaks in synchrotron X-ray diffraction patterns of mimetite-F (Figure 3a) and mimetite-I (Figure 3b) occurred, revealing the presence of a small amount of contamination, different in each of them. They were not detected with other methods. The impurities might have appeared during the synthesis or were simply a contamination. The interpretation of the impurities was not the objective of this study. To improve the refinement parameters and address unidentified peaks on diffraction data of synthesized mimetites, we implemented the approach applied by Baikie et al., [65]. The additional single-phase monoclinic modelling of mimetite-Cl structure was performed (model in $P112_1/b$ [64]). However, the Rietveld refinement did not converge for a monoclinic model. Examination of the peak profiles and comparison with the reflections list of clinomimetite from [64] and [65] indicated, that the peaks resulting from monoclinic structure are missing. Also, unrealistic U_{iso} values were obtained, and the model did not attain convergence. This confirmed decisively that unidentified peaks of minor intensities were negligible and the hexagonal system was an appropriate structural model for the presented lead apatites, and the Rietveld refinement and structural interpretation were successfully performed.

254 **Table 2.** Summary of structural Rietveld refinements of substituted mimetites $Pb_5(AsO_4)_3X$.

Atom		**Parameters**	***X* = F**	***X* = Cl**	***X* = Br**	***X* = I**	***X* = OH**
		a [Å]	10.081	10.249	10.312	10.353	10.187
		c [Å]	7.426	7.443	7.474	7.530	7.523
		V [Å^3]	653.619(8)[a]	677.00(4)	688.320(19)	699.125(24)	676.303(13)
		r$_X$ [Å][b]	1.33	1.81	1.96	2.20	1.37
		Av CR [Å][c]	1.21	1.23	1.24	1.25	1.21
Pb(1)	*x*		1/3	1/3	1/3	1/3	1/3
	y		2/3	2/3	2/3	2/3	2/3
	z		0.00463(14)	0.00506	0.00577(34)	0.00706(27)	0.00357
	*U*iso [Å^2]		0.01415(10)	0.01967	0.02438	0.02871	0.02292
Pb(2)	*x*		0.23638(5)	0.25085	0.25530(12)	0.25888(12)	0.24762
	y		1.00391(9)	1.00362	1.00160(20)	0.99753(19)	0.99940
	z		1/4	1/4	1/4	1/4	1/4
	*U*iso [Å^2]		0.02296(10)	0.01971	0.02286	0.03552	0.03163
As	*x*		0.40395(11)	0.40714	0.40896(20)	0.40491(21)	0.40060
	y		0.38267(10)	0.38331	0.37815(17)	0.380001(17)	0.37689
	z		1/4	1/4	1/4	1/4	1/4
	*U*iso [Å^2]		0.00984(23)	0.00883	0.00838	0.01515	0.01508
O(1)	*x*		0.3208(6)	0.32833	0.34000[h]	0.3567(18)	0.33388
	y		0.4936(5)	0.49474	0.49543[h]	0.5111(14)	0.49738
	z		1/4	1/4	1/4	1/4	1/4
	*U*iso [Å^2]		0.0128(17)	0.04555	0.08219	0.09133	0.02269
O(2)	*x*		0.59886(15)	0.60045	0.60049(23)	0.5960(7)	0.59424
	y		0.4962(5)	0.48128	0.4738(12)	0.4827(12)	0.48179
	z		1/4	1/4	1/4	1/4	1/4
	*U*iso [Å^2]		0.0158(18)	0.02689	0.03885	0.07495	0.06533
O(3)	*x*		0.3518(4)	0.35298	0.3494(10)	0.3591(10)	0.35403
	y		0.2658(4)	0.27245	0.2733(9)	0.2650(9)	0.26182
	z		0.0689(5)	0.06819	0.0636(8)	0.0758(9)	0.07079
	*U*iso [Å^2]		0.0190(13)	0.04534	0.06731	0.11329	0.03906
X	*x*		0	0	0	0	0
	y		0	0	0	0	0
	z		1/2	1/2	1/2	1/2	0.37433
	*U*iso [Å^2]		0.138(7)	0.00555	0.01941	0.025[f]	0.52451
	Occ.[d]		1.012(19)	0.80446	0.797(5)	0.4629(29)	0.86556
	x		-	0[e]	0[e]	0[i]	0[e]
	y		-	0[e]	0[e]	0[i]	0[e]
	z		-	1/2[e]	1/2[e]	1/2[i]	0.37182[e]
	*U*iso [Å^2]		-	0.025[e,f]	0.025[e,f]	0.025[f,i]	0.03003[e,f]
	Occ.		-	0.0535[e]	0.044(5)[e]	0.6150(29)[i]	0.04227[e]
	x		-	0.74971[g]	0.796(5)[g]	-	0.59585[g]
	y		-	0.78630[g]	0.828(5)[g]	-	1.10557[g]
	z		-	0.12045[g]	0.102(5)[g]	-	0.12728[g]
	*U*iso [Å^2]		-	0.025[f,g]	0.025[f,g]	-	0.03003[f,g]
	Occ.		-	0.18841[g]	0.143(14)[g]	-	0.14682[g]
		*wR*p [%]	9.64	7.64	8.38	7.46	9.53
		*R*p [%]	7.67	6.43	7.10	6.28	7.94
		χ^2	3.056	0.901	1.021	1.009	1.918

[a] Numbers in brackets are 1 standard deviation in last significant place(s). [b] Shannon's ionic radii of X-site ion [66]. [c] Average crystal radius = $[(r_{M(1)} \cdot 4) + (r_{M(2)} \cdot 6) + (r_T \cdot 6) + (r_O \cdot 24) + (r_X \cdot 2)]/42$ [5]. [d] Occ. = occupancy. [e] Carbon atom C of CO_3^{2-}. [f] *U*iso not refined. [g] Oxygen atom O(4) of CO_3^{2-}. [h] Value fixed manually to the twist angle refined to 16.38°. [i] OH^- ion incorporated into mimetite-I structure.

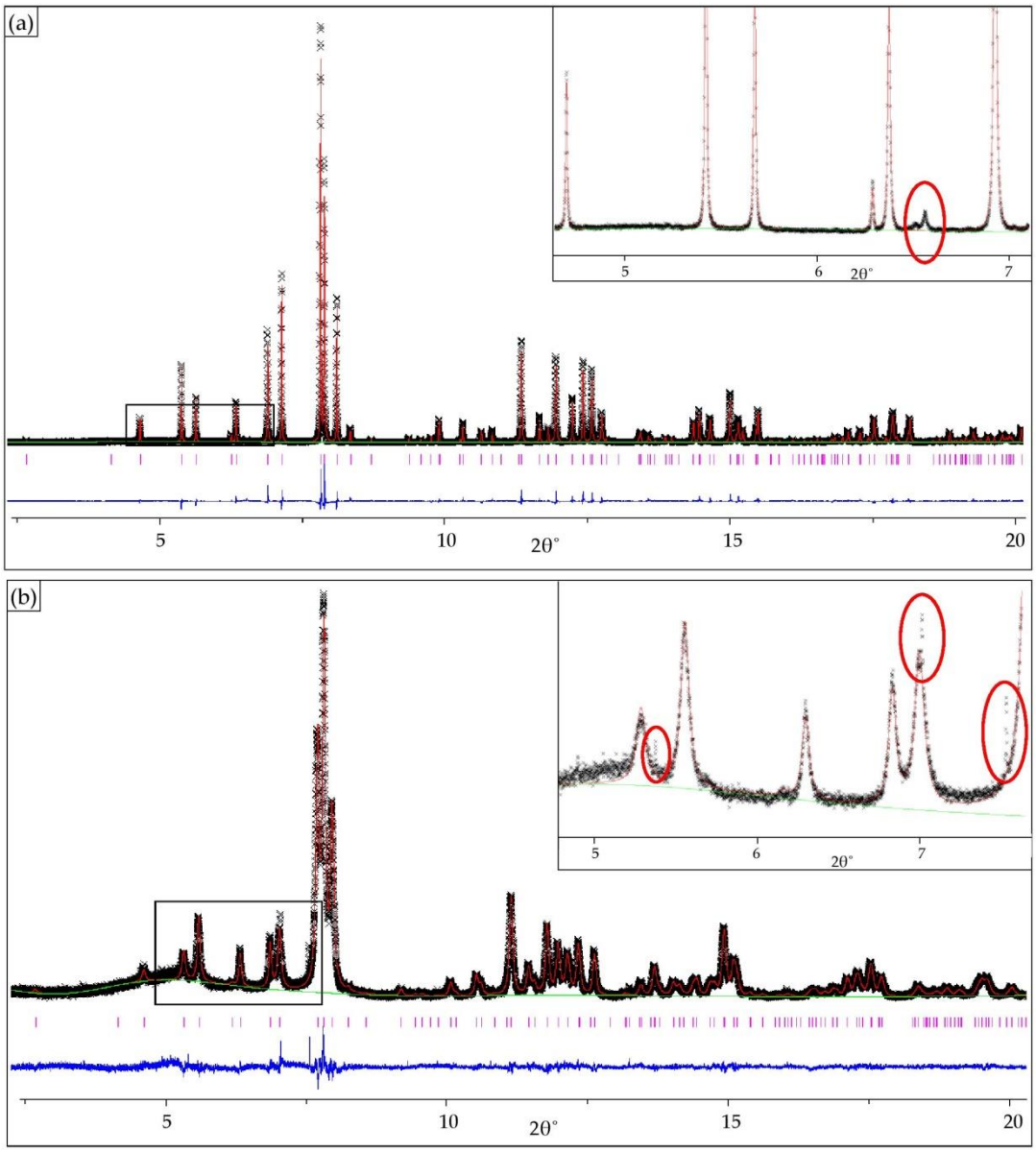

Figure 3. Final observed and calculated synchrotron X-ray powder diffraction patterns for the Rietveld refinements of: **(a)** mimetite-F, and **(b)** mimetite-I with insets displaying tiny peaks from unidentified contaminations (red circles).

4. Discussion

The unit-cell parameters refined for the halogenated mimetites in this study agreed with the references within 0.04 Å (mimetite-F determined by Kreidler and Hummel, [67]; mimetite-Cl determined by Merker and Wondratschek, [16], Henderson et al., [17], Flis et al., [24], and Baikie et al., [63]; mimetite-Br and -I determined by Merker and Wondratschek, [16]; mimetite-OH determined by Kwaśniak-Kominek et al., [27]). Figure 4 presents the dependency between the unit-cell parameters and the halogen's ionic radius. The unit-cell parameters systematically increased with the increase in the substituted halogen's ionic radius (Figure 4a–c). However, the mimetite-OH did not follow the trend. i.e.: the dimensions of the crystalline lattice were higher than

the dimensions predicted based only on the size of the anion. The increase in parameter *a* and unit-cell volume was in line with the nearly ideal linear trend (Figure 4a,c). However, the increase in the width of the unit-cell was almost three times larger than the increase in its height, i.e.: parameter *a* increased by 0.27 Å while parameter *c* increased only by 0.1 Å. Also, mimetite-F did not follow the linear trend of changes in a parameter *c*: the measured value was much higher than the ideal value from the trend delineated by mimetites -Cl, -Br and -I (Figure 4b).

In the hexagonal system, *c*/*a* is the only variable axial ratio. As axial ratios often correspond to the chemical and physical properties in a given structure type, *c*/*a* is one of the key parameters of the $P6_3/m$ apatite structure type. In a study by Mercier et al., [52], large sets of apatite data were compiled, and it was shown that *c*/*a* for apatites extended over a fairly large range from 0.67 to 0.76. The values derived in this study were within this range, and *c*/*a* decreased in the series F-Cl-Br, while the mimetite-I stood out from the linear trend (Figure 4d). The same trend in halogenated mimetites was reported by Merker and Wondratschek, [16]. Moreover, the *c*/*a* ratio for halogenated pyromorphites (calculated based on the unit-cell parameters reported by Kim et al., [11]) also decreased in the same order and displayed a linear trend against the ionic radius of *X*. However, in this study, the *c*/*a* varied very little in the mimetite series, from 0.736 for mimetite-F to 0.724 for mimetite-Br, so the significance of this value is minuscule and may have been overshadowed by the error of determination.

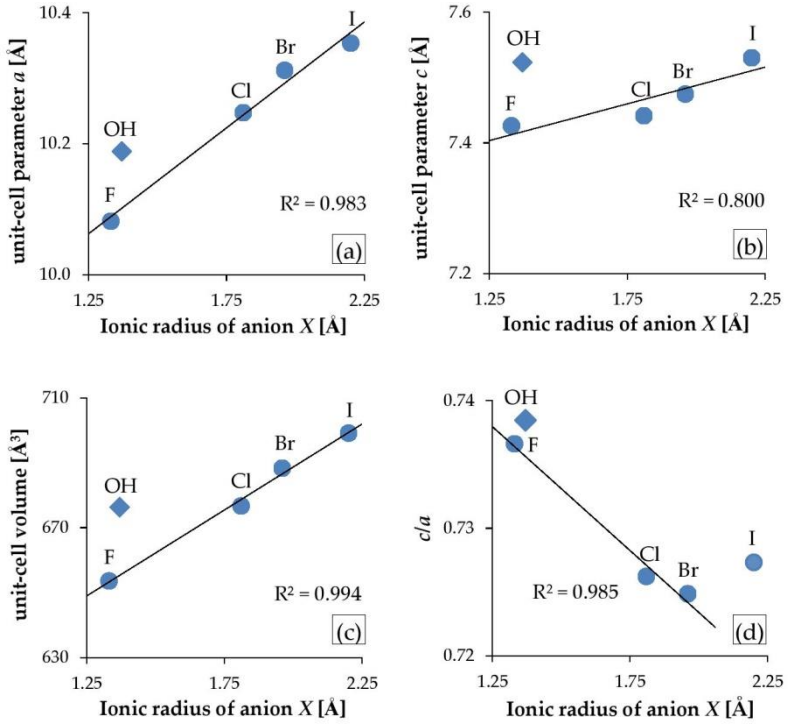

Figure 4. Variation in unit-cell parameters of substituted mimetites: **(a)** parameter *a*, **(b)** parameter *c*, **(c)** unit-cell volume, and **(d)** *c*/*a* ratio, compared with a substituting anion's ionic radius, where ionic radius for F = 1.33 Å, OH = 1.37 Å, Cl = 1.81 Å, Br = 1.96 Å, and I = 2.20 Å. Mimetite-OH (diamonds) does not adhere to the trends.

With the use of pattern recognition and artificial neural networks techniques, Wu et al., [19] revealed that ionic radii predominantly regulate the unit-cell parameters of apatites. They also concluded that there was a strong nonlinear relationship between the unit-cell parameters and the ionic radii. However, our observations based not only on the results of this study but also on existing literature data of selected apatites negate the latter statement. Figure 5 presents the relationship between the unit-cell parameters *a* and *c* as well as the unit-cell volume of selected apatites, and the ionic radii of an anion at the position *X* (F, Cl, Br, I, and OH). Lead, calcium, and strontium phosphates and arsenates were selected: Pb-As apatites from this study; Pb-P and Ca-P apatites after

Kim et al., [11]; $Ca_5(AsO_4)_3OH$ after Lee et al., [68]; $Ca_5(AsO_4)_3F$ according to ICDD card No 23-0112; $Ca_5(AsO_4)_3Cl$ according to ICDD card No 38-0383; $Sr_5(PO_4)_3OH$ after Sudarsanan and Young, [69]; $Sr_5(PO_4)_3F$ after Corker et al., [70]; $Sr_5(PO_4)_3Cl$ after Nötzold et al., [71]; $Sr_5(PO_4)_3Br$ after Alberius-Henning et al., [72]; $Sr_5(AsO_4)_3F$ and $Sr_5(AsO_4)_3Cl$ after Đordević et al., [73]. For all presented series, halogen apatites form linear trends while hydroxyl apatites do not adhere to the pattern: their position is always above the regression line. The unit-cell parameter *a* increases with the increase in halogen's ionic radius (Figure 5a). In contrast, unit-cell parameter *c* decreases with the increase in the ionic radius of *X* except for lead apatites (both phosphates and arsenates), which show an increase in *c* as the size of halogen increases (Figure 5b). The variability of parameter *a* is much greater than parameter *c*. Hence, irrespective of the direction of change of a parameter *c*, in all the series, the volume of a unit-cell increases linearly with the halogen anion's radius (Figure 5c). The results of this study allowed to include the iodine apatite in the calculation for the first time. The phase follows the general linear trend as presented in Figure 5.

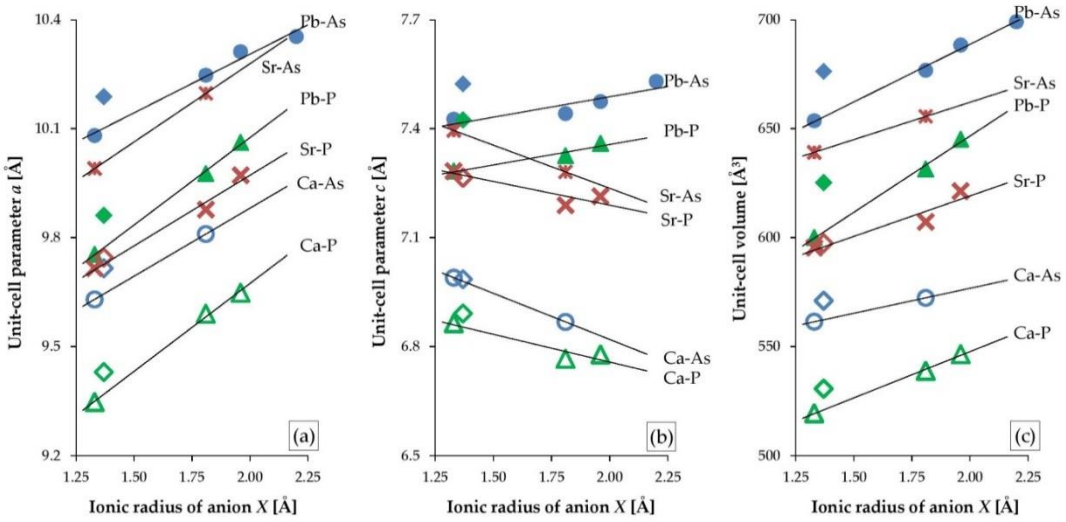

Figure 5. Variations in the unit-cell parameters of substituted apatites based on the results of this study and existing literature ([11,68-73] and ICDD cards No 23-0112 and No 38-0383): **(a)** unit-cell parameter *a*, **(b)** unit-cell parameter *c*, and **(c)** unit-cell volume, compared with a substituting anion's ionic radius, where ionic radius for F = 1.33Å, OH = 1.37Å, Cl = 1.81Å, Br = 1.96Å, and I = 2.20Å.

Of all halogenated mimetites, only the structure of mimetite-Cl has been published [17,63-65,74,75]. Table 3 lists selected interatomic distances and metaprism twist angles of the investigated phases calculated according to the procedure outlined by White and Dong, [2], and the results of the single-crystal X-ray diffraction measurements for mimetite-Cl reported by Dai et al., [64]. For mimetite-Cl, all Pb(1)-O and Pb(2)-O distances, along with the Pb(2)-Cl distance determined in this work agreed with these reported by Dai et al., [64] within 0.07 Å. The As-O bond lengths were restrained to be 1.70(1) Å, 1.71(1) Å, and 1.68(1) Å, respectively, according to those for mimetite-Cl reported by Dai et al., [64].

Table 3. Selected interatomic distances [Å] for substituted mimetites $Pb_5(AsO_4)_3X$. Previously published data for $Pb_5(AsO_4)_3Cl$ are included for comparison.

	This Study					**Dai et al., [64]**
	***X* = F**	***X* = Cl**	***X* = Br**	***X* = I**	***X* = OH**	***X* = Cl**
As-O(1)	1.700	1.696	1.681	1.664(6)	1.674	1.70
As-O(2)	1.709	1.715	1.710	1.715(6)	1.710	1.72
As-O(3)	1.689	1.673	1.679	1.673(4)	1.691	1.67
Average As-O	1.698(9)	1.689(20)	1.687(15)	1.68(1)	1.691(12)	1.69
Distortion index	0.004	0.009	0.006	0.010	0.005	
Pb(1)-O(1)	2.482	2.518	2.564	2.528(5)	2.534	2.52

Pb(1)-O(2)	2.803(4)	2.718	2.685(9)	2.793(9)	2.754	2.78
Pb(1)-O(3)	2.946(4)	3.002	3.054	2.963(9)	2.944	2.94
Pb(2)-O(1)	3.005(5)	3.063	3.137	3.264	3.058	3.07
Pb(2)-O(2)	2.362(4)	2.385	2.421(11)	2.322(10)	2.398	2.33
Pb(2)-O(3)	2.605	2.567	2.514(6)	2.643(7)	2.617	2.63
Pb(2)-O(3)	2.657(4)	2.762	2.831(10)	2.755(10)	2.691	2.73
Pb(2)-X	3.005	3.158	3.222	3.286	2.693	3.16
Twist angle (φ) °	20.34(20)	19.04(26)	16.38(05)	11.42(16)	18.60(26)	18

Systematic structural changes in the studied phases resulted in various linear relationships in the series from mimetite-F to -I. Similar dependencies were found in halogenated pyromorphites reported by Kim et al., [11]. A comparison of selected linear correlations of interatomic distances for halogenated mimetites (from this study) and halogenated pyromorphites [11] are shown in Figure 6. Strong linear correlations were with the anion's ionic radius (Figure 6a–e). Similar trends were also observed with the unit-cell parameter *a* (Figure 6f-j) and with the unit-cell parameter *c* (Figure 6k-o). Linear relations with the anion's ionic radius and with the average crystal radius were identical (data not shown). In most cases, apatites-OH did not follow the linear trends discovered in the series of apatites -F-Cl-Br-I. In mimetites, (As-O) distances within the TO_4 tetrahedra changed to a similarextent as in pyromorphites (P-O), although the As-O bond lengths are significantly greater than the P-O bond lengths (Figure 6a–d,f–i,k–n). Moreover, *T*-O(1) and *T*-O(3) distances decreased in both series. However, As-O(2) distances increased within the mimetite series, which is in contrast to pyromorphites (Figure 6b,g,l). Nevertheless, the average *T*-O distances changed in the same direction in mimetites (As-O) as in pyromorphites (P-O) (Figure 6d,i,n). No obvious relationships between the Pb-O bond distances and unit-cell parameters as well as anion's ionic radius were observed. The Pb(1)-O and Pb(2)-O bond distances in mimetites ranged from 2.321(7) Å to 3.264(0) Å (Table 3). Similar is found in pyromorphites, with the values ranging from 2.359(3) Å to 3.281(4) Å [11]. In overall terms, this indicates that halogen substitutions have similar effect on the structure of mimetites, as on pyromorphites.

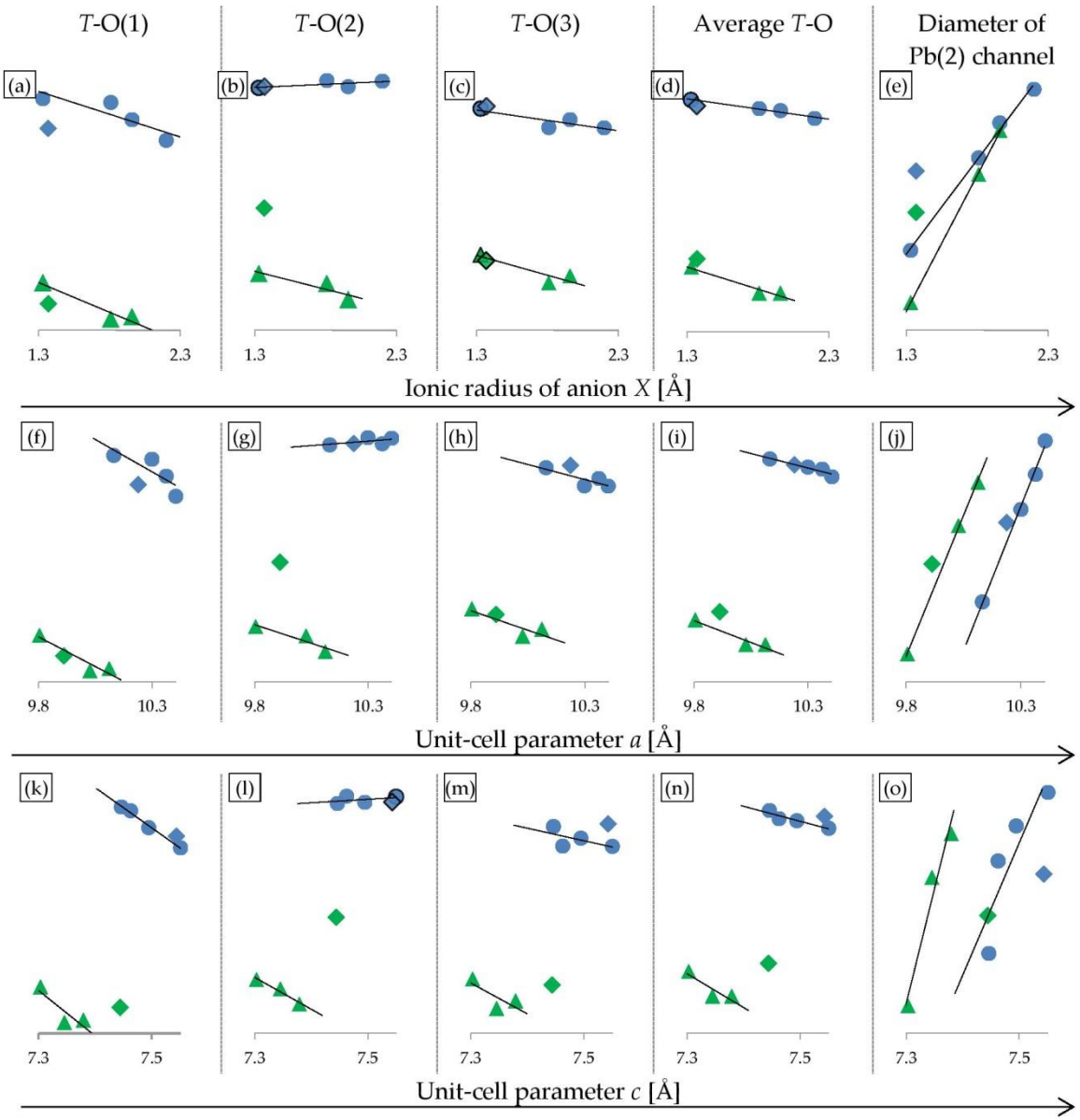

Figure 6. Selected correlations of interatomic distances for halogenated mimetites from this study (blue dots) and halogenated pyromorphites reported by Kim et al., [11] (green triangles). All OH-phases are marked by diamonds: mimetite-OH from this study (blue), and pyromorphite-OH reported by Kim et al., [11] (green). Descriptions in each column head correspond to the vertical axes, and the values are intentionally omitted to highlight the trends within the series (interatomic distances for the mimetite series can be found in Table 3). The horizontal axes are: **(a–e)** ionic radius of anion *X*, **(f-j)** unit-cell parameter *a*, **(k-o)** unit-cell parameter *c*. Ionic radius of anion *X* as well as the unit-cell parameters *a* and *c* increase in the mimetite series F-Cl-Br-I and in the pyromorphite series F-Cl-Br from left to right.

The anions *X* in apatite structures (F^-, Cl^-, Br^-, I^-, OH^-, and on rare occasion, other anions) are positioned within hexagonal channels delineated by rows of *M*(2) cations along the *c* axis [3]. The relationship between the ionic radius of anion *X* and the diameter of the channel can be understood in the (001) projection (Figure 7). In this projection, the diameter of the channel was represented by the distance between opposite *M*(2) cations. The *M*(2) cations formed equilateral triangles perpendicular to the channels. The diameter of the channel was equivalent to the diameter of the circle drawn on such a triangle. Therefore, the diameter of a channel was denoted by the formula (1):

$$d = \frac{2A}{\sqrt{3}} \quad (1)$$

where A referred to a side of a triangle defined by $M(2)$-$M(2)$ distance which can be easily measured in the (001) projection with the use of VESTA or similar crystal structure software.

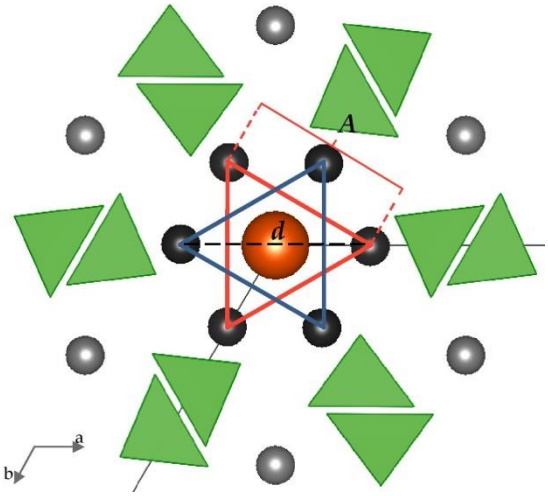

Figure 7. Projection of apatite structure on (001), enabling quantitative determination of the diameter of the channels accommodating *X* anions. Black atoms are Pb(2), grey atoms are Pb(1), an orange atom is *X* anion, and the green triangles are AsO_4 tetrahedra. For clarity, oxygen atoms are not shown, and the size of ions is not set to scale. Both blue and red triangles are formed by Pb(2) cations positioned on the same plane. These triangles are located parallel to each other in the channel.

The hexagonal channel's diameter in the mimetite-F, -Cl, -Br, and -I series increased with an increase in the ionic radius of an anion *X*, although the increase was not proportional: the channel increased at a much slower rate than the ionic radius of anion *X* (Figure 6e). The growth of the channel's diameter was directly proportional to the increase in the unit-cell parameter *a* (Figure 6j). This indicates that the increase of the hexagonal channel's diameter is not directly caused by changes in the size of the ionic radius of the halogen. Halogenated pyromorphites show the same correlation: the diameter of the channel increases in proportion to the increase of the unit-cell parameter *a* and at a slower rate than the increase of the ionic radius of anion *X*, excluding apatites-OH which usually do not follow the trend (Figure 6e,j). This means that in the mimetite-F, -Cl, -Br, and -I series, the successive halogens have less space in the tunnel.

An extremely sensitive structural parameter in apatites is a twist angle φ between the bonds O(1)-M(1)-O(2), which is a twist angle of the $M(1)O_6$ metaprism projected on (001). The value of the twist angle reported to date varies between 60° and 0° and decreases linearly as a function of increasing the average ionic radius of the formula unit [2]. For halogenated mimetites (from this study) and halogenated pyromorphites (reported by White and Dong, [2]), a robust linear relationship was observed not only with the average crystal radius (Figure 8a) but also with unit-cell parameters *a*, and in particular parameter *c* (Figure 8b,c). The latter trend was used as a criterion for the coordinate values of the O(1) atom which were manually adjusted in the Rietveld refinement of the structure of mimetite-Br. The twist angle φ calculated for the halogenated mimetites varied from 20.34° for mimetite-F to 11.42° for mimetite-I. The effect of a decreasing twist angle on the structure of mimetites is visually displayed in Figure 9.

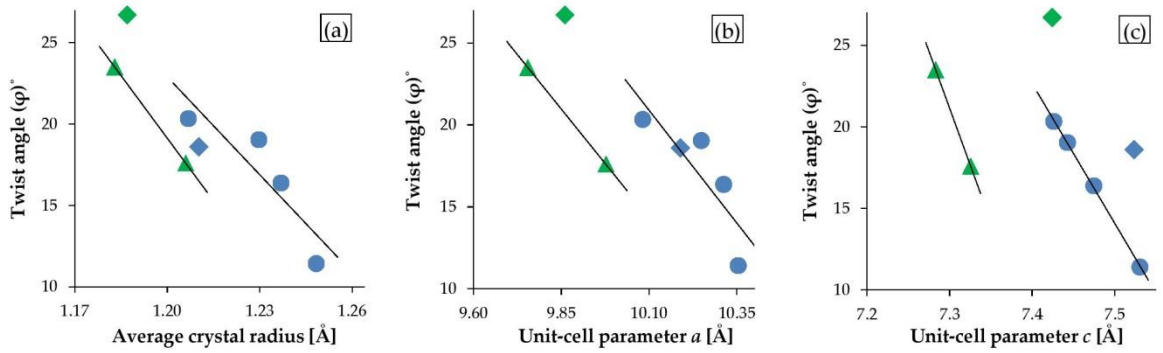

Figure 8. Correlations between metaprism twist angle φ and: **(a)** average crystal radius, **(b)** unit-cell parameter *a*, and **(c)** unit-cell parameter *c*. Halogenated mimetites from this study are denoted by blue dots, and pyromorphites-F and -Cl reported by White and Dong, [2] are denoted by green triangles. All OH- phases are marked by diamonds: mimetite-OH from this study (blue), and pyromorphite-OH reported by White and Dong, [2] (green). Average crystal radius as well as the unit-cell parameters *a* and *c* increase in the mimetite series F-Cl-Br-I and in the pyromorphite series F-Cl from left to right.

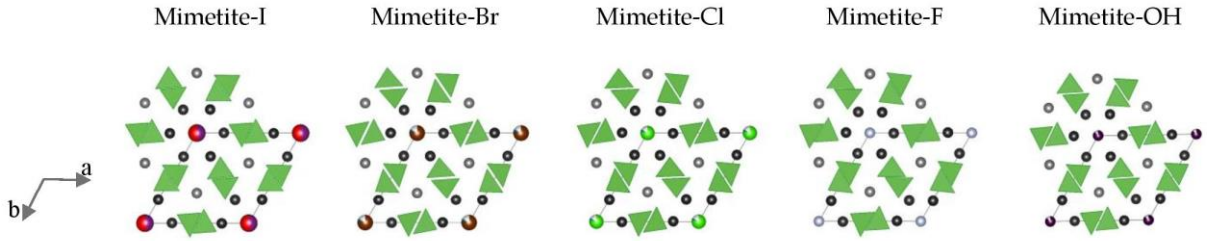

Figure 9. Topological representation of halogenated mimetites projected on (001). Black atoms are Pb(2), grey atoms are Pb(1), and the atoms at the corners of the unit cell represent the (001) projection of the I-Br-Cl-F-OH anion columns. For clarity, oxygen atoms are not shown, and the size of ions is not set to scale. The AsO_4 tetrahedra are emphasized to highlight the effect of twist angle φ.

5. Conclusions

The synthesis of mimetites $Pb_5(AsO_4)_3X$ from aqueous solutions, substituted at the position *X* by F, Cl, Br, I, and OH provided a product with chemical composition consistent with that of the initial solution. This is particularly important for iodine apatites, which have not been studied very widely. Hence, it could be assumed that such apatites may be used in the future for encapsulation of radioactive waste containing ^{129}I.

Rietveld refinement of the synchrotron-based data indicated that all the synthetic mimetites crystallized in the hexagonal system (space group $P6_3/m$, space group number 176). Modelling of the structure in monoclinic space group produced unsatisfactory results. In order to get realistic bond lengths and angles in halogenated mimetite crystalline structures, soft constraints within the TO_4 tetrahedra had to be applied. The systematic structural changes brought about by substitutions of anion *X* determined for the studied mimetite series are similar to the variabilities in the Pb-P- apatite series, and slightly different from the changes observed in the Ca- and Sr- apatites (both arsenates and phosphates). Nevertheless, the significant difference occurs in the inverse trend of the variation of the unit-cell parameter *c*. For most apatites, as the substituted halogen's size increases, the size of the parameter *a* linearly increases and the size of parameter *c* slightly decreases. Since the change in parameter *a* is greater than the change in parameter *c*, a linear increase in the volume of the unit-cell is observed with an increase in the ionic radius of *X*. This variability is different for Pb- apatites: both parameter *a* and parameter *c* increases when a halogen ion with larger radius is substituted. Hence, the linear increase in the unit-cell volume is much sharper for Pb- apatites than for any other apatites. For the first time, iodine mimetite has been included in the calculation, and structural

changes were found to align with the general linear trend. Just like in other apatites series, the structural properties of the hydroxyl phase differed significantly from its halogen counterparts, and the parameters for mimetite-OH did not adhere to the linear correlations determined within the series.

A thorough analysis of the variability of interatomic distances in Pb- apatites considering such a broad range of monovalent anion substitutions was carried out for the first time. An important finding resulting from this analysis is that these substitutions have a similar effect on changes in interatomic distances in mimetites and in pyromorphites. Both, in mimetites and pyromorphites, halogen substitutions caused a small but systematic shortening of the *T*-O distance in the tetrahedron. The increase of the hexagonal channel diameter along with the decrease of the TO_4 tetrahedron size was observed for the successively larger ion placed in the center of the channel: F, OH, Cl, Br, and I, respectively. For the first time, in such a wide range of anionic substitutions, the variability of the metaprism twist angle φ was determined, which is an important structural parameter and a useful device for reviewing changes in apatite topology with changing composition. The φ angle decreased as the substituted halogens's ionic radius increased and the change was almost ideally linear with the unit-cell parameter *c*.

Supplementary Materials: The following are available online at www.mdpi.com/xxx/s1, File S1: Crystallographic Information File of mimetite-F, File S2: Crystallographic Information File of mimetite-Cl, File S3: Crystallographic Information File of mimetite-Br, File S4: Crystallographic Information File of mimetite-I, File S5: Crystallographic Information File of mimetite-OH.

Author Contributions: M.M. designed and supervised this project; J.S. and B.P. performed the experiments; J.S. and M.M. carried out data analysis and calculations; J.S., B.P., M.M., J.T., S.Z.-P., and O.B. wrote the paper. All authors have read and agreed to the published version of the manuscript.

Funding: Financial support for the research was provided to B.P. by the Polish National Science Centre (NCN) grant No. 2017/27/N/ST10/00776.

Acknowledgments: This research used resources of the Advanced Photon Source, a U.S. Department of Energy (DOE) Office of Science User Facility operated for the DOE Office of Science by Argonne National Laboratory under Contract No. DE-AC02-06CH11357. We thank two anonymous experts for their detailed reviews that helped us to improve the manuscript.

Conflicts of Interest: The authors declare no conflict of interests.

References

1. Elliott, J. C.; Wilson, R. M.; Dowker, S. E. P. Apatite structures. *Adv. in X-ray Anal.* **2002**, *45*, 172-181.
2. White, T. J.; Dong, Z. Structural derivation and crystal chemistry of apatites. *Acta Crystallogr. B* **2003,** *59*, 1-16. https://doi.org/10.1107/S0108768102019894
3. White, T.; Ferraris, C.; Kim, J.; Madhavi, S. Apatite–an adaptive framework structure. *Rev. Mineral. Geochem.* **2005**, *57*, 307-401. https://doi.org/10.2138/rmg.2005.57.10
4. Pasero, M.; Kampf, A.R.; Ferraris, C.; Pekov, I.V.; Rakovan, J.; White, T.J. Nomenclature of the apatite supergroup minerals. *Eur. J. Mineral.* **2010**, *22*, 163-179. https://doi.org/10.1127/0935-1221/2010/0022-2022
5. Ptáček, P. *Apatites and their synthetic analogues—synthesis, structure, properties and applications*; InTech: Rijeka, Croatia, 2016. http://dx.doi.org/10.5772/59882
6. Elliott, J.C. *Structure and Chemistry of the Apatites and Other Calcium Phosphates*; Elsevier: Amsterdam, The Netherlands, 1994; ISBN 0-444-81582-1.
7. Hughes, J.M.; Rakovan, J.F. Structurally robust, chemically diverse: apatite and apatite supergroup minerals. *Elements* **2015**, *11*, 165-170. https://doi.org/10.2113/gselements.11.3.165
8. Mackie, P.E.; Elliot, J.C.; Young, R.A. Monoclinic structure of synthetic $Ca_5(PO_4)_3Cl$, chlorapatite. *Acta Crystallogr. B* **1972**, *28*, 1840-1848. https://doi.org/10.1107/S0567740872005114
9. Hata, M.; Marumo, F.; Iwai, S.; Aoki, H. Structure of barium chlorapatite. *Acta Crystallogr. B* **1979**, *35*, 2382-2384. https://doi.org/10.1107/S0567740879009377
10. Hashimoto H.; Matsumoto T. Structure refinements of two natural pyromorphites, $Pb_5(PO_4)_3Cl$, and crystal chemistry of chloroapatite group, $M_5(PO_4)_3Cl$. Z. Kristallogr. **1998**, *213*, 585-590. https://doi.org/10.1524/zkri.1998.213.11.585

11. Kim, J.Y.; Fenton, R.R.; Hunter, B.A.; Kennedy, B.J. Powder diffraction studies of synthetic calcium and lead apatites. *Aust. J. Chem.* **2000**, *53*, 679-686. https://doi.org/10.1071/CH00060
12. Audubert, F.; Savariault, J.M.; Lacout, J.L. Pentalead tris (vanadate) iodide, a defect vanadinite-type compound. *Acta Crystallogr. C* **1999**, *55*, 271-273. https://doi.org/10.1107/S0108270198005034
13. Zhang, M.; Maddrell, E.R.; Abraitis, P.K.; Salje, E.K.H. Impact of leach on lead vanado-iodoapatite [$Pb_5(VO_4)_3I$]: An infrared and Raman spectroscopic study. *Mat. Sci. Eng. B-Adv.* **2007**, *137*, 149-155. https://doi.org/10.1016/j.mseb.2006.11.003
14. Stennett, M.C.; Pinnock, I.J.; Hyatt, N.C. Rapid synthesis of $Pb_5(VO_4)_3I$, for the immobilisation of iodine radioisotopes, by microwave dielectric heating. *J. Nucl. Mater.* **2011**, *414*, 352-359. https://doi.org/10.1016/j.jnucmat.2011.04.041
15. Suetsugu, Y. Synthesis of lead vanadate iodoapatite utilizing dry mechanochemical process. *J. Nucl.* **2014**, *454*, 223-229. https://doi.org/10.1016/j.jnucmat.2014.07.073
16. Merker, L.; Wondratschek, H. Bleiverbindungen mit Apatitstruktur, insbesondere Blei–Jod- und Blei–Brom-Apatite. *Z. Anorg. Allg. Chem.* **1959**, *300*, 41-50. https://doi.org/10.1002/zaac.19593000104
17. Henderson, C.M.B.; Bell, A.M.T.; Charnock, J.M.; Knight, K.S.; Wendlandt, R.F.; Plant, D.A.; Harrison, W.J. Synchrotron X-ray absorption spectroscopy and X-ray powder diffraction studies of the structure of johnbaumite [$Ca_{10}(AsO_4)_6(OH,F)_2$] and synthetic Pb-, Sr- and Ba-arsenate apatites and some comments on the crystal chemistry of the apatite structure type in general. *Mineral. Mag.* **2009**, *73*, 433-455. https://doi.org/10.1180/minmag.2009.073.3.433
18. Epp, T.; Marks, M.A.; Ludwig, T.; Kendrick, M.A.; Eby, N.; Neidhardt, H.; Oelmann, Y.; Markl, G. Crystallographic and fluid compositional effects on the halogen (Cl, F, Br, I) incorporation in pyromorphite-group minerals. *Am. Mineral.* **2019**, *104*, 1673-1688. https://doi.org/10.2138/am-2019-7068
19. Wu, P.; Zeng, Y.Z.; Wang, C.M. Prediction of apatite lattice constants from their constituent elemental radii and artificial intelligence methods. *Biomaterials* **2004**, *25*, 1123-1130. https://doi.org/10.1016/S0142-9612(03)00617-3
20. Markl, G.; Marks, M.A.; Holzäpfel, J.; Wenzel, T. Major, minor, and trace element composition of pyromorphite-group minerals as recorder of supergene weathering processes from the Schwarzwald mining district, SW Germany. *Am. Mineral.* **2014**, *99*, 1133-1146. https://doi.org/10.2138/am.2014.4789
21. Manecki, M.; Maurice, P.A.; Traina, S.J. Uptake of aqueous Pb by Cl−, F−, and OH− apatites: mineralogic evidence for nucleation mechanisms. *Am. Mineral.* **2000**, *85*, 932-942. https://doi.org/10.2138/am-2000-0707
22. Bajda T. Solubility of mimetite $Pb_5(AsO_4)_3Cl$ at 5–55°C. *Environ. Chem.* **2010**, *7*, 268-78. https://doi.org/10.1071/EN10021
23. Borkiewicz, O.; Rakovan, J.; Cahill, C.L. Time-resolved in situ studies of apatite formation in aqueous solutions. *Am. Mineral.* **2010**, *95*, 1224-1236. https://doi.org/10.2138/am.2010.3168
24. Flis, J.; Borkiewicz, O.; Bajda, T.; Manecki, M.; Klasa, J. Synchrotron-based X-ray diffraction of the lead apatite series $Pb_{10}(PO_4)_6Cl_2$–$Pb_{10}(AsO_4)_6Cl_2$. *J. Synchrotron Radiat.* **2010**, *17*, 207-214. https://doi.org/10.1107/S0909049509048705
25. Bajda, T.; Mozgawa, W.; Manecki, M.; Flis, J. Vibrational spectroscopic study of mimetite–pyromorphite solid solutions. *Polyhedron* **2011**, *30*, 2479-2485. https://doi.org/10.1016/j.poly.2011.06.034
26. Janicka, U.; Bajda, T.; Manecki, M. Synthesis and solubility of brompyromorphite $Pb_5(PO_4)_3Br$. *Mineral. Polonica* **2012**, *43*, 129-135. https://doi.org/10.2478/v10002-012-0004-4
27. Kwaśniak-Kominek, M.; Matusik, J.; Bajda, T.; Manecki, M.; Rakovan, J.; Marchlewski, T.; Szala, B. Fourier transform infrared spectroscopic study of hydroxylpyromorphite $Pb_{10}(PO_4)_6OH_2$ –hydroxylmimetite $Pb_{10}(AsO_4)_6(OH)_2$ solid solution series. *Polyhedron* **2015**, *99*, 103-111. https://doi.org/10.1016/j.poly.2015.07.002
28. Puzio, B.; Manecki, M.; Kwaśniak-Kominek, M. Transition from Endothermic to Exothermic Dissolution of Hydroxyapatite $Ca_5(PO_4)_3OH$–Johnbaumite $Ca_5(AsO_4)_3OH$ Solid Solution Series at Temperatures Ranging from 5 to 65°C. *Minerals* **2018**, *8*, 281. https://doi.org/10.3390/min8070281
29. Ma, Q.Y.; Traina, S.J.; Logan, T.J.; Ryan, J.A. In situ lead immobilization by apatite. *Environ. Sci. Technol.* **1993**, *27*, 1803-1810. https://doi.org/10.1021/es00046a007
30. Xu, Y.; Schwartz, F.W. Lead immobilization by hydroxyapatite in aqueous solutions. *J. Contam. Hydrol.* **1994**, *15*, 187-206. https://doi.org/10.1016/0169-7722(94)90024-8
31. Ma, Q.Y.; Logan, T.J.; Traina, S.J. Lead immobilization from aqueous solutions and contaminated soils using phosphate rocks. *Environ. Sci. Technol.* **1995**, *29*, 1118-1126. https://doi.org/10.1021/es00004a034

32. Ma, L.Q. Factors influencing the effectiveness and stability of aqueous lead immobilization by hydroxyapatite. *J. Environ. Qual.* **1996**, *25*, 1420-1429. https://doi.org/10.2134/jeq1996.00472425002500060036x
33. Laperche, V.; Traina, S.J.; Gaddam, P.; Logan, T.J. Chemical and mineralogical characterizations of Pb in a contaminated soil: reactions with synthetic apatite. *Environ. Sci. Technol.* **1996**, *30*, 3321-3326. https://doi.org/10.1021/es960141u
34. Laperche, V.; Logan, T.J.; Gaddam, P.; Traina, S.J. Effect of apatite amendments on plant uptake of lead from contaminated soil. *Environ. Sci. Technol.* **1997**, *31*, 2745-2753. https://doi.org/10.1021/es961011o
35. Kumpiene, J.; Lagerkvist, A.; Maurice, C. Stabilization of As, Cr, Cu, Pb and Zn in soil using amendments–a review. *Waste Manag.* **2008**, *28*, 215-225. https://doi.org/10.1016/j.wasman.2006.12.012
36. Liang, Y.; Cao, X.; Zhao, L.; Arellano, E. Biochar- and phosphate-induced immobilization of heavy metals in contaminated soil and water: implication on simultaneous remediation of contaminated soil and groundwater. *Environ. Sci. Pollut.* **2014**, *21*, 4665-4674. https://doi.org/10.1007/s11356-013-2423-1
37. Zeng, G.; Wan, J.; Huang, D.; Hu, L.; Huang, C.; Cheng, M.; Xue, W.; Gong, X.; Wang, R.; Jiang, D. Precipitation, adsorption and rhizosphere effect: the mechanisms for phosphate-induced Pb immobilization in soils—a review. *J. Hazard. Mater.* **2017**, *339*, 354-367. https://doi.org/10.1016/j.jhazmat.2017.05.038
38. Manecki, M. Lead in Water and Soil: Speciation, Toxicity, and Treatment Technologies. In *Encyclopedia of Water: Science, Technology, and Society*; Maurice, P.A.; Willey, 2020; pp. 1713-1727 ISBN: 978-1-119-30075-5.
39. Harrison, W.J.; Wendlandt, R.F.; Wendlandt, A.E. Low temperature aqueous solubility and stability of apatite-structure arsenates of lead, barium, and strontium and uptake of arsenic by hydroxylapatite. International Mineralogical Association, 18th General Meeting, Edinburgh, Scotland , September 1-6, 2002; Abstract A18-10, pp.185.
40. Wendlandt, A.E.; Harrison, W.J.; Wendlandt, R.F. Investigation of hydroxylapatite as a means of removing dissolved arsenic from potable water. Geological Society of America Annual Meeting, Denver, Colorado, USA, October 27-31, 2002.
41. Harrison, W.J.; Wendlandt, R.F.; Charnock, J.M.; Henderson, C.M.B. Spectroscopic investigations of the adsorption of As onto bovine bone. In *Geochimica et Cosmochimica Acta*, *69*, 15th Annual Goldschmidt Conference, Idaho, USA, May 21-25, 2005; pp. A65.
42. Bundschuh, J.; Holländer, H.M.; Ma, Q. *In-situ remediation of arsenic-contaminated sites;* CRC Press: Boca Raton, USA, 2017; pp. 208. ISBN 9781138747753
43. Rakovan, J.F.; Hughes, J.M. Strontium in the apatite structure: strontian fluorapatite and belovite-(Ce). *Can. Mineral.* **2000**, *38*, 839-845. https://doi.org/10.2113/gscanmin.38.4.839
44. Ewing, R.C. The design and evaluation of nuclear-waste forms: clues from mineralogy. *Can. Mineral.* **2001**, *39*, 697-715. https://doi.org/10.2113/gscanmin.39.3.697
45. Pan, Y.; Fleet, M.E. Compositions of the apatite-group minerals: substitution mechanisms and controlling factors. *Rev. Mineral. Geochem.* **2002**, *48*, 13-49 https://doi.org/10.2138/rmg.2002.48.2
46. Rakovan, J.; Reeder, R.J.; Elzinga, E.J.; Cherniak, D.J.; Tait, C.D.; Morris, D.E. Structural characterization of U(VI) in apatite by X-ray absorption spectroscopy. *Environ. Sci. Technol.* **2002**, *36*, 3114-3117. https://doi.org/10.1021/es015874f
47. Luo, Y.; Hughes, J.M.; Rakovan, J.; Pan, Y. Site preference of U and Th in Cl, F, and Sr apatites. *Am. Mineral.* **2009**, *94*, 345-351. https://doi.org/10.2138/am.2009.3026
48. Audubert, F.; Carpena, J.; Lacout, J.L.; Tetard, F. Elaboration of an iodine-bearing apatite iodine diffusion into a $Pb_3(VO_4)_2$ matrix. *Solid State Ionics* **1997**, *95*, 113-119. https://doi.org/10.1016/S0167-2738(96)00570-X
49. Uno, M.; Kosuga, A.; Masuo, S.; Imamura, M.; Yamanaka, S. Thermal and mechanical properties of $AgPb_9(VO_4)_6I$ and $AgBa_9(VO_4)_6I$. *J. Alloys Compd.* **2004**, *384*, 300-302. https://doi.org/10.1016/j.jallcom.2004.04.094
50. Campayo, L.; Grandjean, A.; Coulon, A.; Delorme, R.; Vantelon, D.; Laurencin, D. Incorporation of iodates into hydroxyapatites: a new approach for the confinement of radioactive iodine. *J. Mater. Chem.* **2011**, *21*, 17609-17611. https://doi.org/10.1039/C1JM14157K
51. Yao, T.; Lu, F.; Sun, H.; Wang, J.; Ewing, R.C.; Lian, J. Bulk iodoapatite ceramic densified by spark plasma sintering with exceptional thermal stability. *J. Am. Ceramic Soc.* **2014**, *97*, 2409-2412. https://doi.org/10.1111/jace.13101

52. Mercier, P.H.; Le Page, Y.; Whitfield, P.S.; Mitchell, L.D.; Davidson, I.J.; White, T.J. Geometrical parameterization of the crystal chemistry of $P6_3/m$ apatites: comparison with experimental data and *ab initio* results. *Acta Crystallogr. B* **2005**, *61*, 635-655. https://doi.org/10.1107/S0108768105031125
53. Vegas, A.; Jansen, M. Structural relationships between cations and alloys; an equivalence between oxidation and pressure. *Acta Crystallogr. B* **2002**, *58*, 38-51. https://doi.org/10.1107/S0108768101019310
54. Mercier, P.H.; Le Page, Y.; Whitfield, P.S.; Mitchell, L.D. Geometrical parameterization of the crystal chemistry of $P6_3/m$ apatite. II. Precision, accuracy and numerical stability of the crystal-chemical Rietveld refinement. *J. Appl. Cryst.* **2006**, *39*, 369-375. https://doi.org/10.1107/S0021889806009903
55. Baker, W.E. An X-ray diffraction study of synthetic members of the pyromorphite series. *Am. Mineral.* **1966**, *51*, 1712–1721
56. Marciniak, H.; Diduszko, R.; Kozak, M. *XRAYAN. Program do Rentgenowskiej Analizy Fazowej, Wersja 4.0.1*; Koma: Warszawa, Poland, 2006. (In Polish)
57. Holland, T.J.B.; Redfern, S.A.T. UNITCELL: a nonlinear least-squares program for cell-parameter refinement and implementing regression and deletion diagnostics. *J. App. Cryst.* **1997**, *30*, 84. https://doi.org/10.1107/S0021889896011673
58. Larson, A.C.; Von Dreele, R.B. *General structure analysis system*. Report LAUR 86-748; Los Alamos National Laboratory, NM, USA, 1994.
59. Toby, B.H. *EXPGUI*, a graphical user interface for *GSAS*. *J. Appl. Cryst.* **2001**, *34*, 210-213. https://doi.org/10.1107/S0021889801002242
60. Momma, K.; Izumi, F. VESTA 3 for three-dimensional visualization of crystal, volumetric and morphology data. *J. Appl. Cryst.* **2011**, *44*, 1272-1276.
61. Young, R.A. *The Rietveld method*; Oxford University Press: New York, NY, USA, 1993; pp. 298
62. Dai, Y.; Hughes, J.M. Crystal structure refinements of vanadinite and pyromorphite. *Can. Mineral.* **1989**, *27*, 189-192.
63. Baikie, T.; Ferraris, C.; Klooster, W.T.; Madhavi, S.; Pramana, S.S.; Pring, A.; Schmidt, G.; White, T.J. Crystal chemistry of mimetite, $Pb_{10}(AsO_4)_6Cl_{1.48}O_{0.26}$, and finnemanite, $Pb_{10}(AsO_3)_6Cl_2$. *Acta Crystallogr. B* **2008**, *64*, 34-41. https://doi.org/10.1107/S0108768107066402
64. Dai, Y.; Hughes, J.M.; Moore, P.B. The crystal structure of mimetite and clinomimetite, $Pb_5(AsO_4)_3Cl$. *Can. Mineral.* **1991**, *29*, 369-376.
65. Baikie, T.; Schreyer, M.; Wei, F.; Herrin, J.S.; Ferraris, C.; Brink, F.; Topolska, J.; Piltz, R.O.; Price, J.; White, T.J. The influence of stereochemically active lone-pair electrons on crystal symmetry and twist angles in lead apatite-2*H* type structures. *Mineral. Mag.* **2014**, *78*, 325-345. https://doi.org/10.1180/minmag.2014.078.2.07
66. Shannon, R.D. Revised effective ionic radii and systematic studies of interatomic distances in halides and chalcogenides. *Acta crystallogr. A* **1976**, *32*, 751-767. https://doi.org/10.1107/S0567739476001551
67. Kreidler, E.R.; Hummel, F.A. The crystal chemistry of apatite: structure fields of fluor- and chlorapatite. *Am. Mineral.* **1970**, *55*, 170-184.
68. Lee, Y.J.; Stephens, P.W.; Tang, Y.; Li, W.; Phillips, B.L.; Parise, J.B.; Reeder, R.J. Arsenate substitution in hydroxylapatite: structural characterization of the $Ca_5(PxAs_{1-x}O_4)_3OH$ solid solution. *Am. Mineral.* **2009**, *94*, 666-675. https://doi.org/10.2138/am.2009.3120
69. Sudarsanan, K.; Young, R.A. Structure of strontium hydroxide phosphate, $Sr_5(PO_4)_3OH$. *Acta Crystallogr. B* **1972**, *28*, 3668-3670. https://doi.org/10.1107/S0567740872008544
70. Corker, D.L.; Chai, B.H.T.; Nicholls, J.O.H.N.; Loutts, G.B. Neodymium-Doped $Sr_5(PO_4)_3F$ and $Sr_5(VO_4)_3F$. *Acta Crystallogr. C* **1995**, *51*, 549-551. https://doi.org/10.1107/S0108270194006906
71. Nötzold, D.; Wulff, H.; Herzog, G. Differenzthermoanalyse der Bildung des Pentastrontiumchloridphosphats und röntgenographische Untersuchung seiner Struktur. *J. Alloys Compd.*, **1994**, *215*, 281-288. https://doi.org/10.1016/0925-8388(94)90855-9
72. Alberius-Henning, P.; Mattsson, C.; Lidin, S. Crystal structure of pentastrontium tris(phosphate) bromide, $Sr_5(PO_4)_3Br$ and of pentabarium tris(phosphate) bromide $Ba_5(PO_4)_3Br$, two bromoapatites. *Z. Kristallogr. NCS* **2000**, *215*, 345-346. https://doi.org/10.1515/ncrs-2000-0319
73. Đordević, T.; Šutović, S.; Stojanović, J.; Karanović, L. Sr, Ba and Cd arsenates with the apatite-type structure. *Acta Crystallogr. C* **2008**, *64*, i82-i86. https://doi.org/10.1107/S0108270108023457
74. Calos, N.J.; Kennard, C.H.; Davis, R.L. Crystal structure of mimetite, $Pb_5(AsO_4)_3Cl$. *Z. Kristallogr. Cryst. Mater.* **1990**, *191*, 125-130. https://doi.org/10.1524/zkri.1990.191.14.125

642 75. Okudera, H. Relationships among channel topology and atomic displacements in the structures of
643 Pb5(BO4)3Cl with B = P (pyromorphite), V (vanadinite), and As (mimetite). *Am. Mineral.* **2013**, *98*,
644 1573-1579. https://doi.org/10.2138/am.2013.4417

645